INTERNATIONAL JOURNAL FOR NUMERICAL METHODS IN BIOMEDICAL ENGINEERING
Int. J. Numer. Meth. Biomed. Engng. (2013)
Published online in Wiley Online Library (wileyonlinelibrary.com). DOI: 10.1002/cnm.2556

Multiphysics computational models for cardiac flow and virtual cardiography

Jung Hee Seo, Vijay Vedula, Theodore Abraham and Rajat Mittal*,†

Johns Hopkins University, 3400 N Charles St, Baltimore, MD 21218, USA

SUMMARY

A multiphysics simulation approach is developed for predicting cardiac flows as well as for conducting virtual echocardiography (ECHO) and phonocardiography (PC) of those flows. Intraventricular blood flow in pathological heart conditions is simulated by solving the three-dimensional incompressible Navier–Stokes equations with an immersed boundary method, and using this computational hemodynamic data, echocardiographic and phonocardiographic signals are synthesized by separate simulations that model the physics of ultrasound wave scattering and flow-induced sound, respectively. For virtual ECHO, a Doppler ultrasound image is reproduced through Lagrangian particle tracking of blood cell particles and application of sound wave scattering theory. For virtual PC, the generation and propagation of blood flow-induced sounds ('hemoacoustics') is directly simulated by a computational acoustics model. The virtual ECHO is applied to reproduce a color M-mode Doppler image for the left ventricle as well as continuous Doppler image for the outflow tract of the left ventricle, which can be verified directly against clinically acquired data. The potential of the virtual PC approach for providing new insights between disease and heart sounds is demonstrated by applying it to modeling systolic murmurs caused by hypertrophic cardiomyopathy. Copyright © 2013 John Wiley & Sons, Ltd.

Received 12 November 2012; Revised 11 February 2013; Accepted 8 April 2013

KEY WORDS: hemodynamics; hemoacoustics; echocardiography; phonocardiography; computational fluid dynamics; Doppler ultrasound; hypertrophic cardiomyopathy; systolic murmur

1. INTRODUCTION

Computational modeling has increasingly become the tool of choice for studying cardiac flows [1–6]. Computational modeling of hemodynamics enables a comprehensive analysis of flow, pressure, vorticity, and other flow related metrics in normal as well as diseased hearts and, in doing so, may reveal the significance of flow structures for ventricular function. The future of computational hemodynamics is the simulation of flows in patient-specific models (e.g. [2, 4]) for improved diagnostic assessment and modeling assisted treatment and surgery.

A number of issues and challenges exist in order to achieve this promise of computational hemodynamics of cardiac flows. This paper deals with two of these challenges: the first one is the need for methods to rapidly assess the validity of the computational result for a patient-specific simulation. It should be noted that although simulations of cardiac flows can be validated and verified for canonical (benchtop) models, the translation of these models into clinical practice will require revalidation for each and every patient. This is primarily because the input data (such as inflow/outflow conditions) obtained from the patient specific measurements for the simulation oftentimes are limited and some of these need to be estimated or modeled. Thus, the overall accuracy of the computational result for every patient-specific model needs to be validated prior to using the simulation data for

---

*Correspondence to: Rajat Mittal, Johns Hopkins University, 3400 N Charles St, Baltimore, MD 21218, USA.

†E-mail: mittal@jhu.edu

diagnosis and treatment. The second issue addressed here is the connection between the computational hemodynamic results and the diagnostic data used in the clinical field. Although the flow features and vortical structures can be investigated in detail with the computational hemodynamics, it is currently difficult to use this information directly for the diagnosis and treatment for the heart diseases. Therefore, it may be important to develop correlations between specific features of cardiac flows (as extracted from computational fluid dynamics (CFD)) and the clinical data that are available for diagnosis of cardiac function.

The aforementioned two issues can be addressed by generating 'virtual' cardiographies using the computational hemodynamic results of cardiac flows. In this study, we describe a multiphysics simulation approach for the modeling of cardiac flows as well as virtual echocardiography (ECHO) and phonocardiography (PC). Cardiac ECHO employs Doppler ultrasound for the assessment of intracardiac flows (e.g., [7–9]), and PC employs recording and analysis of heart sounds for auscultation [10–13]. Both ECHO and PC are noninvasive and inexpensive diagnostic methods for cardiac disease and oftentimes used to diagnose and assess heart conditions including but not limited to diastolic dysfunction, valvular disease, congenital disorders, and cardiomyopathies. For example, the early/atrial filling wave velocity ratio (E/A ratio) measured by the pulsed wave (PW) Doppler [8] and the flow propagation velocity extracted from the color M-mode Doppler diagram [14] are used to assess the health of the ventricle. In addition to this, continuous wave (CW) Doppler is applied to check the severity of aortic stenosis or sub-aortic obstacle based on the maximum blood flow velocity in the outflow tract [9]. At the same time, the blood flow in the ventricle with diastolic dysfunction (e.g., very high ($>>1$) or low ($<<1$) E/A ratios) causes additional heart sounds such as the so-called S3 and S4 sounds [13], and heart murmur [10] is generated by abnormal blood flows associated with aortic stenosis, obstructive hypertrophic cardiomyopathy (HCM), and mitral regurgitation.

All the diagnostic metrics extracted from ECHO Doppler investigation and abnormal heart sounds are directly related to the blood flow dynamics in the ventricle. Thus, virtual ECHO and PC can serve as a bridge between clinical data and computational hemodynamic results. In the present study, intraventricular blood flows for left ventricles (LVs) with pathological conditions (diastolic dysfunction, HCM) are simulated via CFD, and echocardiographic and phonocardiographic data are synthesized by separate simulations that model the physics of ultrasound wave scattering and flow-induced sound, respectively. These 'virtual' ECHO and PC provide data that can be compared directly with clinically acquired data. In particular, these virtual ECHO and PC can be used for rapid validation of computational results by comparing to the actual cardiographic data, and furthermore, such comparisons will allow us to calibrate a given patient-specific, computational heart model. The virtual cardiography will also improve our ability to interpret the cardiac flow simulation data. It is expected that the development of detailed correlations between blood flow dynamics and the cardiographic data will provide valuable information for the improvement of diagnostic tools based on these modalities. The simulation methods are described in Section 2, and in Section 3, we describe the simulations of blood flow inside LV with severe diastolic dysfunction and the associated mitral inflow Doppler and color M-mode Doppler. We also describe virtual modeling of CW Doppler measurements for the LV outflow tract and the systolic ejection murmur associated with obstructive HCM.

2. METHODS

In the present study, intraventricular blood flow is simulated by solving the three-dimensional incompressible Navier–Stokes equations with an immersed boundary method [15]. Using this computational hemodynamic result, virtual echocardiographies and phonocardiographies are generated via separate simulations that model the physics of ultrasound wave scattering and flow-induced sound, respectively. For virtual ECHO, we generate Doppler ultrasound images which depicts intraventricular flow motions. This is carried out by Lagrangian tracking of particles and applying sound wave scattering theory [16] to these particles. The Lagrangian particles represent virtual red blood cells (RBCs) that are primarily responsible for the backscatter of ultrasound from blood. The motion of virtual RBC particles is tracked by using the time-dependant Eulerian velocity field obtained from the cardiac flow simulation, and ultrasound wave propagation and scattering by RBC particles are described by an acoustic analogy for arbitrary transducer/receiver shape. Once the time series of scattered ultrasound signal is obtained on the receiver, a Doppler ultrasound image can be constructed by a signal processing approach.

For virtual PC, we simulate the blood flow-induced sound generation and propagation (‘hemoacoustics’) using a hybrid approach that employs the incompressible Navier–Stokes and the linearized perturbed compressible equations (LPCE) [17]. The sound source term in this approach is obtained from the computational hemodynamic simulation, and the sound propagation through the thorax is modeled with a structural wave equation.

2.1. *Computational hemodynamics*

For the intraventricular blood flows, blood is assumed to be a Newtonian fluid and thus its motion is governed by the incompressible Navier–Stokes equations;

$$\nabla \cdot \vec{U} = 0, \quad \frac{\partial \vec{U}}{\partial t} + (\vec{U} \cdot \nabla)\vec{U} + \frac{1}{\rho_0}\nabla \vec{P} = \nu_0 \nabla^2 \vec{U}, \tag{1}$$

where $\vec{U}$ is a velocity vector, P is a pressure, and ρ_0 and ν_0 are the density and kinematic viscosity of the blood. Equation (1) is solved by a fractional step method [18];

$$\frac{\vec{U}^* - \vec{U}^n}{\Delta t} = \frac{1}{2}\left[-(\vec{U} \cdot \nabla)\vec{U} + \nu_0 \nabla^2 \vec{U}\right]^* + \frac{1}{2}\left[-(\vec{U} \cdot \nabla)\vec{U} + \nu_0 \nabla^2 \vec{U}\right]^n, \tag{2}$$

$$\nabla^2 P^{n+1} = \frac{\rho_0}{\Delta t}\nabla \cdot \vec{U}^* \tag{3}$$

$$\vec{U}^{n+1} = \vec{U}^* - \frac{\Delta t}{\rho_0}\nabla P^{n+1} \tag{4}$$

where $\vec{U}^*$ is a intermediate velocity field and superscript n denotes the time level. The advection–diffusion equation, Equation (2), is computed by a second-order Crank–Nicolson method, and the pressure Poisson equation, Equation (3), is solved by a geometric multi-grid method [19]. All the spatial derivatives are discretized by a second-order central differencing. The discretized equations are solved on the nonbody conformal Cartesian grid and the complex, moving boundaries are treated by a sharp-interface immersed boundary method as described in Ref. [15]. In this method, the endocardial surface is represented by an unstructured mesh with triangular elements, and this surface is immersed into the Cartesian volume grid. The key difference between the present immersed boundary method and the previous work of Peskin and coworkers [20, 21] is that the boundary condition on the immersed body surface is directly imposed by assigning the variable value on the ‘Ghost cell’ (the cell in the nonfluid region adjacent to the fluid cell) rather than applying a distributed forcing term on the momentum equation (Equation (2)). Also, we do not solve the elastic fiber equations for the myocardium. In the present study, the endocardial surface moves with a prescribed velocity, and the boundary conditions for the flow field on the surface are imposed by a multi-dimensional ghost-cell method. Further details of the present immersed boundary flow solver can be found in the Ref. [15].

2.2. *Blood cell particle tracking*

The motion of ‘virtual’ RBCs is simulated by the Lagrangian particle tracking algorithm. The particles that represent the RBC are randomly distributed in the blood flow domain, and their motion is tracked by the equation

$$\vec{x}_p(t + \Delta t) = \vec{x}_p(t) + \int_t^{t+\Delta t} \vec{U}(\vec{x}_p)\, \mathrm{d}t, \tag{5}$$

DOI: 10.1002/cnm

where $\vec{x}_p$ is the particle position vector and $\vec{U}(\vec{x})$ is the Eulerian velocity vector field obtained from the full Navier–Stokes computation. The velocity at the particle position is computed by a tri-linear interpolation and the time integration of Equation (5) is performed by a four-stage Runge–Kutta method.

2.3. *Doppler ultrasound modeling*

In this study, we model the scattering of ultrasound wave by each RBC as proposed by Oung and Forsberg [16]. The schematic diagram is shown in Figure 1. The ultrasound wave emitted from the transducer surface (S_1) propagates to the moving RBC particle and the wave scattered by the particle is received by the receiver surface (S_2). Note that two surfaces S_1 and S_2 can be the same. The ultrasound wave emitted by a transducer of arbitrary shape can be modeled by a Green's function solution [22] as

$$\psi(\vec{x},t) = \frac{1}{2\pi}\int_S \frac{1}{r} e(t - r/c)\,\mathrm{d}S, \tag{6}$$

where ψ is a velocity potential of the sound wave, r is the distance from the point on the transducer surface to $\vec{x}$, c is the speed of sound, and $e(t)$ is the surface normal velocity fluctuation signal. The surface integral (S) is for the transducer surface. If we assume that the sound wave is reflected spherically by the rigid small particle, the signal received by the receiver surface is given by the reciprocity relation [16] as

$$s_n(t) = \frac{R}{(2\pi)^2}\int_{S_2}\int_{S_1} \frac{1}{r_2(\mu)}\frac{1}{r_1(\mu)} e(\mu - r_1(\mu)/c)\,\mathrm{d}S_1\,\mathrm{d}S_2, \tag{7}$$

where s_n is the signal received by the receiver surface for a single particle, $\mu = t - r_2/(c - v\cos\theta)$, and R is a constant reflection coefficient.

The Doppler signal can be generated (i.e., extraction of the frequency shifting) by performing a direct sampling [16] of received signal $s_n(t)$ at $t_s = t_g + kT$, where t_s is the sampling time, t_g is the sampling start time, k is an integer, and T is the period of original signal, $e(t)$. Also, to add phase information on the sampled signal, a complex signal [16] can be constructed as

$$\tilde{s}_n(t_s) = \frac{R}{(2\pi)^2}\int_{S_2}\int_{S_1} \frac{1}{r_2(\mu_s)}\frac{1}{r_1(\mu_s)} \tilde{e}(\mu_s - r_1(\mu_s)/c)\,\mathrm{d}S_1\,\mathrm{d}S_2, \tag{8}$$

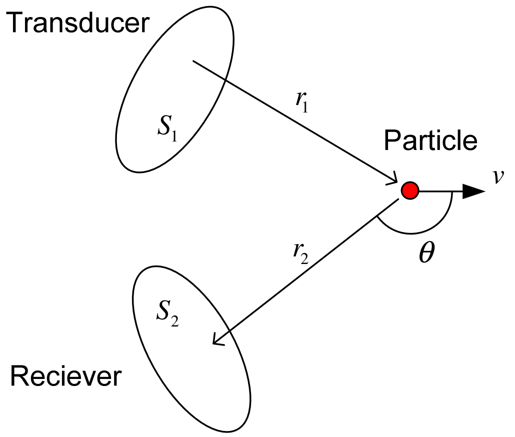

Figure 1. Schematic of Doppler ultrasound modeling.

where $\mu_s = t_s - r_2/(c - v\cos\theta)$, $\tilde{e}(t) = e(t) + i\,e'(t)$, and $e'(t)$ is the Hilbert transform of $e(t)$. The frequency shifting on the received signal, Δf, can be found by the Fourier transform of the sampled, complex signal, $\tilde{s}_n(t_s)$, and the frequency shifting is related with the particle velocity as

$$\Delta f = \frac{2v\cos\theta}{c - v\cos\theta} f_0 \simeq \frac{2v\cos\theta}{c} f_0, \tag{9}$$

where $f_0\ (= 1/T)$ is the frequency of original signal, $e(t)$. In this study, the transducer/receiver surface is represented by triangular surface meshes, and the surface integrals in Equation (8) are evaluated by using the trapezoidal rule. The received signal for all the RBC particles in the blood volume can then be represented by

$$\tilde{s}(t_s) = \sum_{n=1}^{N} \tilde{s}_n(t_s), \tag{10}$$

where N is the total number of particles. Here, we neglected the effect of multiple scattering by assuming R is small (i.e., weak scattering). The spectral analysis of $\tilde{s}(t_s)$ gives the velocity information of the target blood volume based on Equation (9), and this is the basis of the Doppler ultrasound image construction.

For a CW Doppler in which $e(t)$ is given by a continuous periodic function, the Doppler ultrasound image can be constructed by the time-frequency spectrogram of signal, $\tilde{s}(t_s)$. For example,

$$S(t, \Delta f) = |FT(\tilde{s}(\tau) \cdot w(t - \tau))|^2, \tag{11}$$

where FT denotes the Fourier transform and w is a window function [23]. The frequency, Δf, can be converted to the velocity by Equation (9), and one obtains the energy distribution in a 2D space, $S(t,v)$, which shows the time variations of the velocity (distribution) for the target blood volume. Note that CW scans all the blood volume that lies on the path of ultrasound wave beam. For a PW Doppler, a transducer emits the pulses of wave packet for the duration of T_d (pulse duration) with the time interval, T_p (pulse repeating period). At a given time, PW scans the blood volume located at the specific distance (d) from the transducer. If we sample the received signal using the pulse repeating period, T_p, as a sampling time interval, the distance, d, is related with the sampling start time, t_g, by

$$d = t_g c/2. \tag{12}$$

Thus, for a PW, one can obtain multiple samples and spectrograms for the different t_g, and each one of them corresponds to the blood volume at the specific distance, d. From those spectrograms, one can find the representative velocity of the blood volume at the given distance (d) and time (t) based on the maximum energy level of the spectrogram, and consequently construct the velocity field in a 2D space, that is, $V(t,d)$. A color M-mode [7] can be constructed by plotting this velocity field with color contours in a 2D space.

2.4. *Computational hemoacoustics*

The sound generated by blood flow in the heart is simulated with an immersed boundary method-based hybrid approach. First, the hemodynamic flow field inside the heart is simulated with the immersed boundary incompressible Navier–Stokes flow solver described earlier, and the flow-induced sound generation and propagation are modeled by the LPCE [17]. The incompressible Navier–Stokes/LPCE hybrid method is a two-step, one-way coupled approach for the prediction of flow-induced sound at low Mach numbers [17, 24, 25]. Because the heart sound is generally auscultated on the chest (precordium) surface, the sound propagation through the thorax is also modeled by a linear structural wave equation. The LPCE and a linear wave equation are fully coupled by combining them into a single set of equations, and the different material domains are treated by varying the material properties. A unified single set of acoustic equations are written as [26]

$$\begin{aligned} \frac{\partial \vec{u}'}{\partial t} + H(\vec{x})\nabla(\vec{u}\cdot\vec{U}) + \frac{1}{\rho(\vec{x})}\nabla p' = 0, \\ \frac{\partial p'}{\partial t} + H(\vec{x})[(\vec{U}\cdot\nabla)p' + (\vec{u}'\cdot\nabla)P] + K(\vec{x})(\nabla\cdot\vec{u}') = -\frac{DP}{Dt}H(\vec{x}), \end{aligned} \tag{13}$$

where ($\prime$) represents the compressible (acoustic) perturbation, H is a Heaviside function that has a value of 1 in the blood flow region and 0 elsewhere, and the density (ρ) and bulk modulus ($K = \rho c^2$) are functions of space. The capital letters (U, P) indicate the hydrodynamic incompressible variables and they are obtained from the incompressible flow simulations (Equations 1–4).

By solving Equation (13), the wave transmission and reflection at the interface between the blood flow and tissue are automatically resolved based on the difference of acoustic impedance $Z = K/c$. In this model, the propagation of shear waves in the tissue material is not considered, because the shear modulus of the tissue materials is much smaller than the bulk modulus [27]. Also, the dissipation of the acoustic wave is neglected because the frequency range of the heart sound is typically low (∼O(100) Hz), and the dissipation for these low frequencies is expected to be very small. The current fluid-like assumption of the tissue material for the purpose of resolving acoustic wave propagation has been widely used for the simulation of sound wave propagation in biological materials [27–29]. The present approach has also been used for the direct computation of arterial bruits [26]. Equation (13) is discretized in space with a fourth-order compact finite difference scheme [30] and integrated in time using a four-stage Runge–Kutta method. A second-order Lagrangian interpolation [25] is used for the temporal interpolation of flow variables.

3. RESULT AND DISCUSSION

3.1. *Left ventricle model*

We have constructed a simplified model of the LV based on the high-resolution, multi-detector contrast CT scan of the LV. Figure 2(a) shows the model and some geometrical parameters. In this study, we use $D_{M1} = 2.4$ cm, $D_{M2} = 2.0$ cm, $D_A = 2.0$ cm, $D_{LV} = 3.75$ cm, $L_{LV} = 6.5$ cm, and the resulting end-systole ventricle volume is 56 ml. Although the mitral and aortic valve motions are not simulated, we mimic the opening and closure of those valves by changing the boundary conditions of the LV model for the diastole and systole phases. For the diastole phase, the aorta is blocked at

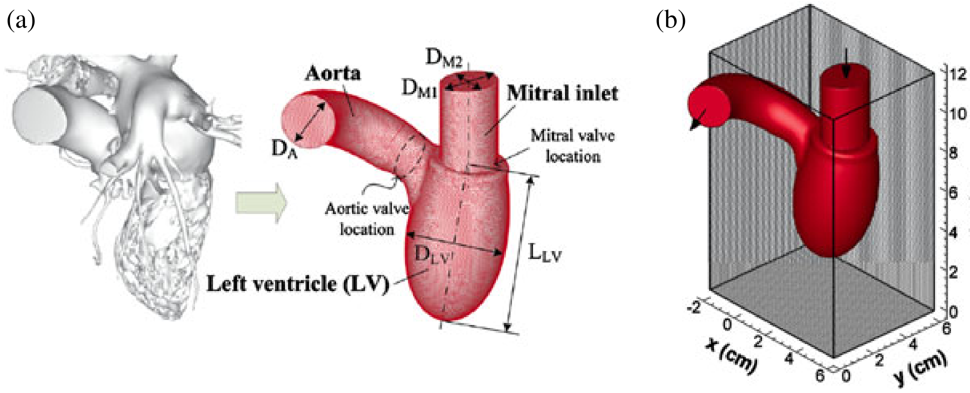

Figure 2. (a) Three-dimensional model of the left ventricle of a human adult. Left: real left ventricle model extracted from a contrast CT scan. Right: a simplified model used for the intraventricular flow simulation. The model consists of 37,256 triangular mesh elements. (b) Computational domain and Cartesian grid for the blood flow simulation. A grid with 256 × 256 × 384 grid points is used and every fourth grid point is plotted here. Velocity boundary conditions are applied on the nodes of the endocardial surface grid, and the pressure boundary conditions are applied at the mitral inlet and aorta exit.

DOI: 10.1002/cnm

the aortic valve location, whereas the mitral inlet is blocked at the mitral valve location during the systole phase. The blood volume flow rate through the mitral inlet (diastole) or the aorta (systole) is modeled based on the previous study [31]. A blood flow rate profile (see Figure 3(a)) is given by

$$Q(t) = \begin{cases} -Q_E \frac{1}{2}\left(1 - \cos\frac{2\pi t}{t_{EE}}\right) & \text{for } 0 \leqslant t \leqslant t_{EE} \\ -Q_A \frac{1}{2}\left(1 - \cos\frac{2\pi (t - t_{AS})}{t_{AE} - t_{AS}}\right) & \text{for } t_{AS} \leqslant t \leqslant t_{AE} \\ Q_S \frac{1}{2}\left(1 - \cos\frac{\pi (t - t_{SS})}{t_{SP} - t_{SS}}\right) & \text{for } t_{SS} \leqslant t \leqslant t_{SP} \\ Q_S \frac{1}{2}\left(1 + \cos\frac{\pi (t - t_{SP})}{t_{SE} - t_{SP}}\right) & \text{for } t_{SP} \leqslant t \leqslant t_{SE} \\ 0 & \text{otherwise} \end{cases}, \tag{14}$$

where Q_E, Q_A, and Q_S are the peak flow rate for E-wave, A-wave, and systolic ejection, respectively, and these parameters should satisfy the relation $Q_E t_{EE} + Q_A(t_{AE} - t_{AS}) = Q_S(t_{SE} - t_{SS})$ for volume conservation. A negative value of the flow rate indicates ventricular filling, and positive value is for the blood ejected to the aorta. In this study, the heart rate is assumed to be 60 BPM (i.e., the duration of one heart cycle is 1 s), and we use the following parameters: $Q_E = 314$ ml, $Q_A = 0.5Q_E$, $t_{EE} = 0.3$ s, $t_{AS} = 0.45$ s, $t_{AE} = 0.64$ s, $t_{SS} = 0.68$ s, $t_{SP} = 0.78$ s, and $t_{SE} = 0.98$ s [31,33]. These parameters yield the stroke volume of 62 ml, an ejection fraction equal to 53%, and the E/A ratio based on the peak volume averaged velocity is 2. This E/A ratio corresponds to the condition of 'restrictive filling' that is found in late-stage diastolic dysfunction [34] and is chosen to investigate the blood flow pattern and the characteristics of the Doppler echocardiograms. For the reference, the blood flow wave form of the normal condition (E/A = 1.2 [34]) for the same stroke volume and ejection fraction is also plotted in Figure 3(a). The LV motion (expansion and contraction) is prescribed by satisfying the volume flow rate given previously in a similar fashion with the previous work of Taylor *et al.* [35], and the time variation of LV volume is plotted in Figure 3(b)

3.2. Intraventricular hemodynamics

The aforementioned LV model is represented by the unstructured surface mesh of 37,256 triangular elements (see Figure 2(a)), and this surface mesh is immersed in the Cartesian volume mesh that covers a cuboidal domain of size 8 × 6 × 12 cm (Figure 2(b)). At the boundaries of inlet (mitral inlet) and exit (aorta), the pressure is specified and the zero-normal-gradient condition is applied for the velocities. To suppress numerical instabilities caused by the back-flow at the outflow boundaries, we used the back-flow-stabilization boundary condition suggested by Moghadam *et al.* [36] on these boundaries. A no-slip, no-penetration boundary condition is applied on the ventricular wall. For the present case, the Reynolds number based on the mitral inlet diameter (D_{M1}) and the peak volume averaged velocity through the mitral inlet is about 4000 which is inline with an adult human heart. We have employed three different grids to assess grid dependence: 64 × 64 × 128 (A),

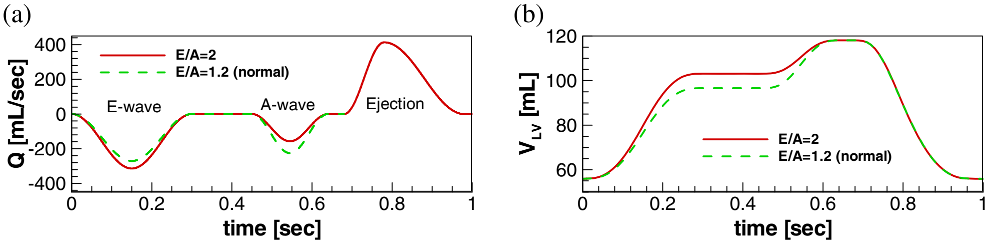

Figure 3. (a) Blood flow rate profile for the left ventricle model and (b) time variation of the left ventricle volume, V_{LV}, for diastolic dysfunction (E/A = 2) and normal (E/A = 1.2) conditions.

DOI: 10.1002/cnm

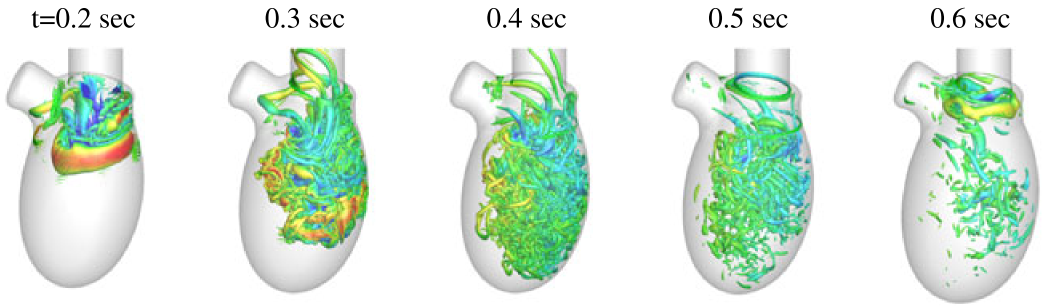

Figure 4. Time evolution of intraventricular vortical structure during diastole. The vortical structures are visualized by the second invariant of velocity gradient [32] (iso-surface of the value 20,000 s^{-2}) and colored by the axial (along the center line of mitral inlet) velocity.

$128 \times 128 \times 256$ (B), and $256 \times 256 \times 384$ (C). Although grid A produces results that are slightly different from those obtained on grids B and C, these last two grids generate results (velocity profiles, vorticity patterns, and pressure distributions) that have very little quantifiable difference. Nevertheless, we use the finest resolution grid C (total 25 million grid points) for our computational study in order to ensure that any grid effects are negligible. The intraventricular flow fields obtained by solving Equations (2–4) are visualized in Figures 4 and 5. For the clear visualization of diastolic flow patterns and vortex structures, we plotted the result of the first cycle since in the first cycle, the diastolic vortices move into a quiescent flow which is devoid of vortices that are remnant from previous cycles.

Figure 4 shows the time evolution of vortical structure during diastole. At t=0.2 s, a vortex ring generated by the incoming blood flow of the E-wave (Figure 3) is clearly observed. The vortex ring is slightly tilted in the counter-clockwise direction, because the convection speed of the right hand side of the vortex ring is slowed down by the interaction with the lateral wall of the ventricle. Because of this interaction with the wall and the relatively high Reynolds number, the vortex ring rapidly becomes unstable and starts to breakdown (0.3 s). The vortex ring is completely broken into small eddies and is indicative of a transitional flow during late diastole (0.4 s) and the small eddies are also observed to dissipate rapidly. At 0.6 s, another weaker vortex ring is generated by the incoming flow associated with the A-wave. Although we have not shown here, the normal E/A ratio condition (E/A = 1.2) also shows the similar vortical structures (vortex ring formation and breakdown to smaller structure), except that the E-wave jet is slightly weaker and the A-wave jet is a little bit stronger than the present case, which one can expect from Figure 3(a).

The flow patterns in the ventricle are visualized in Figure 5 by the vorticity contours and velocity vectors on the long-axis plane for whole heart cycle. At t=0.2 s, one can see that the right-hand side vortex is decaying due to the interaction with the wall, while the left-hand side vortex becomes dominant. Thus the vortical flows move toward the lateral wall, and the overall intraventricular flow exhibits a clockwise circulation. The E-wave vortex breaks and dissipates during diastole (0.3–0.5 s). The incoming flow of the A-wave goes primarily to the lateral wall due to the interaction with the clockwise circulation and a small vortex ring is formed near the mitral annulas during the deceleration of the A-wave ($t = 0.6$ s). The overall clockwise circulation pattern is still observed during early systole (0.7 s), and due to this, the velocity strength near the septal wall is bit stronger during the ejection. The overall intraventricular flow pattern is similar to the results of previous studies [5, 6, 31, 37, 38] but, by using a high-resolution computational grid, we observe smaller scale flow structures that are not reported previously.

3.3. *Particle tracking*

The RBC motions are modeled via Lagrangian particle tracking and the motion of these particles is used for the Doppler ultrasound simulation. Initially, a total of 6000 massless point particles that represent RBCs are randomly distributed in the ventricle, and the particle motion is computed by

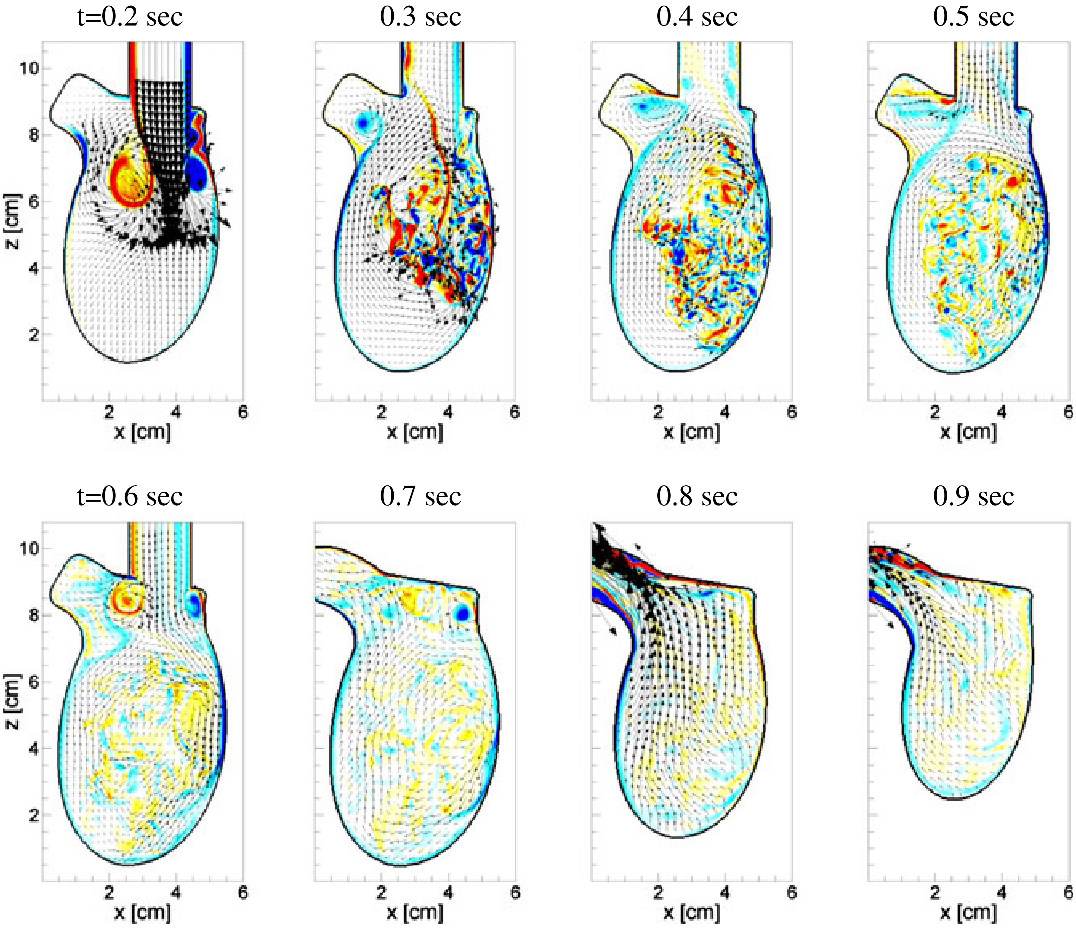

Figure 5. Vorticity contours and velocity vectors at the cross-section for whole heart cycle. Color contour denotes y-component voriticy and the every eighth vectors are plotted.

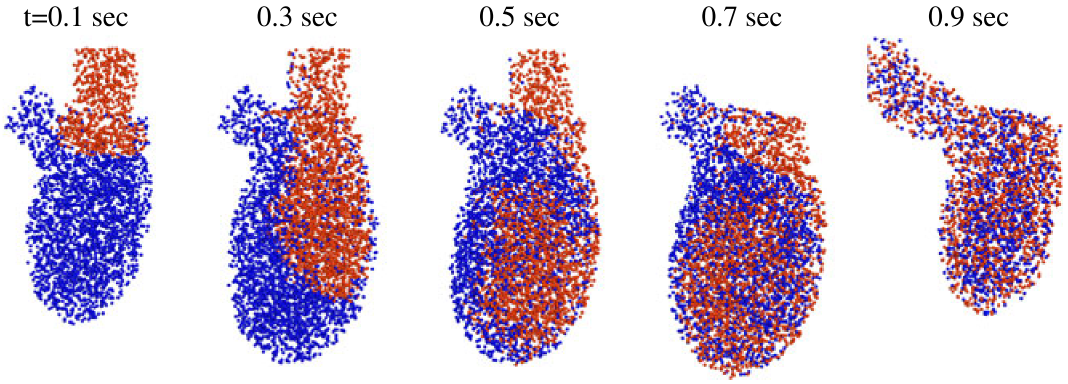

Figure 6. Distribution of RBCs computed by a Lagrangian particle tracking. Red: atrial RBCs, Blue: ventricular RBCs.

solving Equation (5). The particles are continuously injected though the mitral inlet during diastole, and the particles exiting the aorta during systole are removed. The RBC particle distributions during the cardiac cycle are shown in Figure 6. To examine the transport of RBCs, the particles that enter through the mitral inlet into the ventricle are tagged as ‘atrial’ RBCs (and colored red) and the RBC

DOI: 10.1002/cnm

residing in the ventricle at the beginning of diastole are tagged as ‘ventricular’ RBC (and colored blue). One can see the mixing of these two RBC groups by the ventricular vortices. The position and velocity of each RBC particle are saved for the Doppler ultrasound computation described in the next section. We note that the particle tracking can also be used for the analysis of ventricular washout and blood residence time in the LV.

3.4. Doppler ultrasound simulation

For modeling the propagation of the ultrasound wave, we employed a transducer/receiver (transducer hereafter) of rectangular, parabolic shape. The size of the transducer is 2 × 1 cm (Figure 7(a)) and the distance to the focus point of the parabola is 3 cm. Note however that the current approach allows us to use an ultrasound wave transducer of any shape. The main driving frequency (f) of ultrasound in our modeled transducer is 2 MHz, which is in the range of medical ultrasound frequency. As shown in Equation (9), a higher driving frequency results in a larger frequency shifting, thereby making it easier to detect small velocity changes. In the computer simulation, however, because there is virtually no lower limit to the detecting frequency shift, the choice

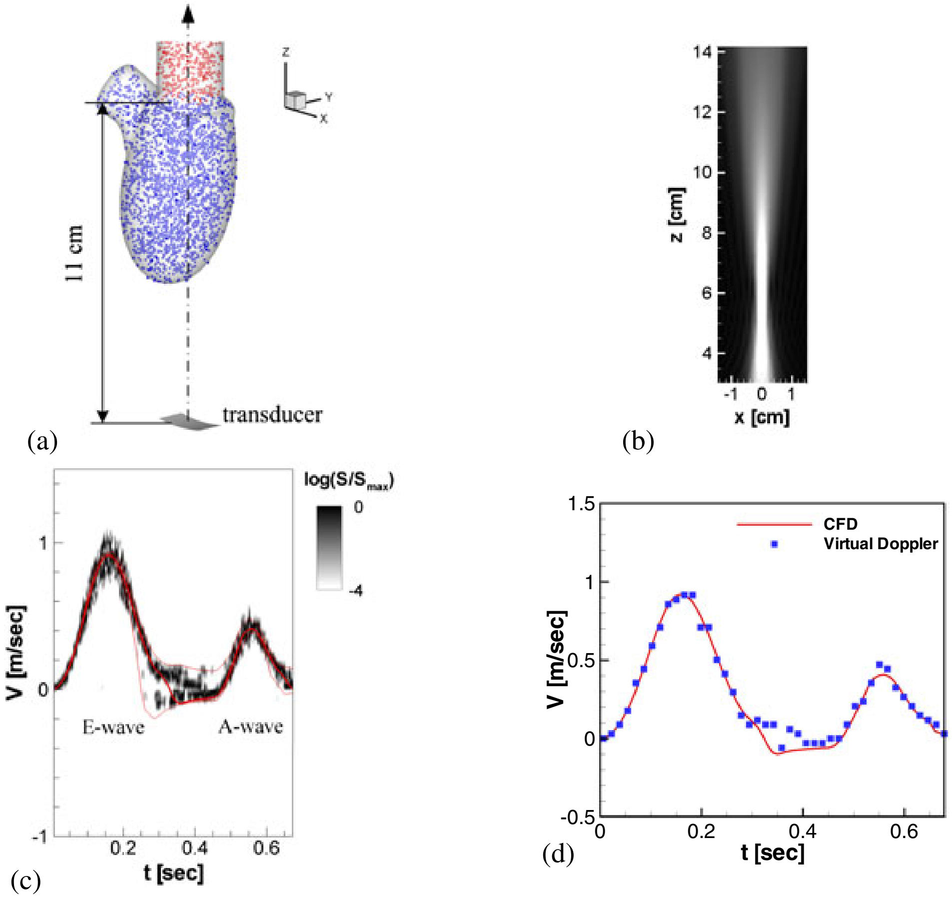

Figure 7. (a) Transducer position and the direction of ultrasound wave beam for the mitral inflow diagram and color M-mode. (b) Root-mean-squared velocity potential field for the current transducer. The coordinates are centered at the center of transducer. (c) Simulated mitral inflow diagram. The thick red line indicates the actual mitral centerline velocity obtained from the flow field simulation result, and thin red lines are the maximum and minimum velocities in the sample volume of Doppler ultrasound obtained from the computational fluid dynamics (CFD) result. (d) Comparison of temporal velocity profile at the mitral inlet; solid line: mitral centerline velocity from CFD, symbols: temporal profile of representative velocity based on the maximum energy intensity on the spectrogram of virtual Doppler simulation.

DOI: 10.1002/cnm

of driving frequency does not play an important role. The more important parameter in the Doppler ultrasound simulation is the sampling frequency,(f/k,where k is an integer) because the sampling frequency limits the range of detected velocity which is given by $|v| \leqslant c/(4k)$. Here, we use k ranging from 100 to 200 and the maximum range of detected velocity is ±3.75 (m/s) which is large enough to resolve intraventricular flow velocity.

A key feature of the ultrasound transducer model is the discretization of the transducer surface. In the current simulations, it is discretized by 160 triangular elements for the computation and each element acts as a point source of ultrasonic energy. If the number of surface elements (number of point sources) is too small, the resulting ultrasound field becomes irregular and nonuniform, while too many elements significantly increase the computational time because the computational cost is proportional to the square of the number of elements. The present number of surface elements provides a smooth ultrasound field with reasonable computational time. For example, the computation of M-mode Doppler with 40 volume samples takes about 12 hours using 40 CPUs. The root mean squared velocity potential of sound wave emitted by the current transducer computed by Equation (6) is plotted in Figure 7(b). With the present setup, the distance from the transducer to the focal point (the point of maximum intensity) is about 6 cm, and the ventricle is placed at the focal and far-field region. The Doppler ultrasound simulations are performed by Equations (8) and (10) using the RBC particle motions shown above.

The model of ultrasound is first used in a pulsed Doppler mode to extract the mitral inflow velocity from our CFD model. The mitral inflow diagram shows the temporal velocity profile through the mitral inlet and is used to determine the clinically important parameters such as the E/A ratio and the E-wave deceleration time [8]. In the current computational study, the transducer is located at the center of mitral inlet and 11 cm below from the mitral valve location. The ultrasound wave beam is perfectly aligned with the mitral inlet axis (z-dir). The pulse duration is 1 μs and the pulse repeating frequency is 10 kHz. The target sample volume is at a distance of 11 cm from the transducer (i.e., mitral valve location). The mitral inflow diagram is obtained from the spectrogram of the received signal (Equation 11) and plotted in Figure 7(c). In this figure, the thick red line indicates the actual velocity at the mitral center line obtained directly from the flow simulation and thin red lines are the minimum and maximum velocities in the sample volume of Doppler ultrasound. Grayscale contours represent the normalized energy intensity, $S(t,V)/S_{max}(t)$ of the scattered ultrasound wave signal received by the transducer. Here $S_{max}(t)$ is the maximum energy intensity at the given time instance. Thus the diagram shows the distributions of the velocity detected by the Doppler ultrasound and the velocity value corresponding to the maximum energy intensity, S_{max} can be considered as the representative velocity of the sample volume.

We note that the temporal variation of the mitral inflow velocity evaluated by the Doppler ultrasound agrees well with the actual velocity profile. Because the ultrasound scans the volume of blood flow instead of a point and the blood flow velocities in that volume are not constant, the velocity obtained by the Doppler ultrasound is slightly dispersed around the actual velocity at a point but it is bounded well by the actual maximum and minimum velocities in the sample volume, except around the peak of E-wave. The overestimated dispersion of velocity value at around the E-wave peak may be caused by the signal processing. Specifically, for higher velocity (i.e., higher Δf), the number of time sampling point per wavelength decreases, and this will cause the energy dispersion but it can be resolved by increasing the sampling rate. We note however that the representative velocity profile conforms very well with the centerline velocity profile from the CFD as shown in Figure 7(d) and this verifies the present velocity measurement procedure using the Doppler ultrasound simulation. Although we imposed an E/A ratio of 2 based on the volume averaged peak velocity for the E and A waves, the E/A ratio evaluated from Figure 7(c) based on the velocity value of maximum energy intensity at the peaks of E and A waves is 0.918(m/s)/0.406(m/s)=2.26. This suggests the potential of the current virtual ECHO model to help identify possible sources of error in Doppler based velocity measurements. Because we already know the exact velocity value and the current Doppler ultrasound modeling excludes all the sources of uncertain errors (e.g. external noise, effects of tissue Doppler, and etc.), the present ECHO model can be used to investigate the effects of signal processing, duty-cycle and sampling frequencies, and transducer type and geometry.

DOI: 10.1002/cnm

The assessment of mitral inflow velocity using the virtual ECHO will also help the validation and calibration of a patient specific heart model for cardiac flow simulations. Because the mitral inflow is in fact the inflow boundary condition, the ventricular flow pattern will be very sensitive to the mitral inflow profile. If one perform the virtual ECHO using the same transducer type, driving and sampling frequencies, and ultrasound wave beam direction with the actual ECHO, the virtual ECHO data can directly be compared to the actual one, and based on that, one can validate or calibrate the patient specific computational heart model. For example, if the magnitude of inflow velocity is not matched, it means that the volume change rate of the LV model is incorrect. This would not be a rare situation especially if the patient-specific heart model would be based on functional (4D) CT scans which typically do not have a high temporal sampling rate (e.g. 12 frames for a cycle). Thus, the ECHO data based calibration will improve the reliability of patient specific heart models.

Next, the virtual ECHO is used in the color M-mode to produce diastolic wave velocity patterns. The transducer position and properties of PW ultrasound are the same with the above case, and the velocity field of the second cardiac cycle ($1 \leqslant t \leqslant 2$ (s)) is used. The velocities for a total of 40 sample volumes are extracted from the apex to the mitral annulus and the spatial resolution of sampling is 2 mm. The resulting color M-mode image is shown in Figure 8(a). Here a positive velocity indicates flow toward the transducer, that is, from the mitral to the apex. Figure 8(b) shows the similar plot made by using the z-direction velocity values directly obtained from the flow field computation and it shows very good correlation with the simulated color M-mode Doppler plot. This comparison also proves that the direct velocity data from CFD can be used as the surrogate of color M-mode diagram [6, 31]. Note that, however, the direct CFD data cannot incorporate the effects of ultrasound and transducer parameters. In Figure 8(a), one can see the propagation of blood flow which comes into the ventricle with the E and A waves. The propagation velocity of blood flow, v_p, is usually evaluated by the slope of the velocity contour (based on the contour at 50% of the maximum velocity [7]) on the color M-mode image and used as a parameter to estimate the ventricle function [14]. In the present case, the propagation velocity for the E-wave is estimated to be about 31 cm/s (black solid line in Figure 8(a)) which is in the range (37±12 cm/s) reported by Garcia *et al.* [7] for human study with 14 elderly patients (age: 64±11). It has been reported that v_p is about 70 cm/s for the normal ventricle with physiological E/A ratio but it decreases to about 24 cm/s for low or high E/A ratios [14]. Another index suggested for the assessment of ventricular function is v_E/v_p, where v_E is the peak velocity of E-wave, and $v_E/v_p > 1.5$ for the diseased ventricles [14]. For the present case, the conditions correspond to severe diastolic dysfunction with E/A=2 and v_E/v_p yields 2.96. However, a proper way to determine the propagation velocity, v_p, is still arguable [39]. With the current computational hemodynamics and Doppler ultrasound simulation approach, it is possible to investigate the correlation between the evaluated propagation velocity based on the color M-mode and the actual blood transportation velocity, and also the correlation between the

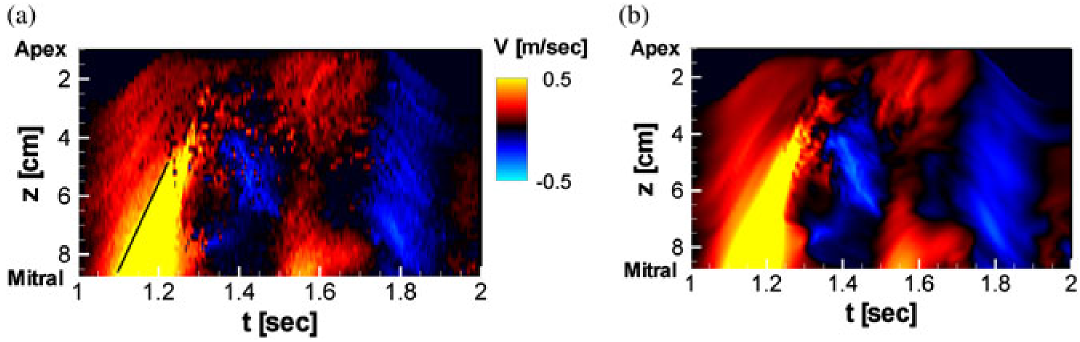

Figure 8. Temporal velocity variation along the mitral center line. (a) Simulated color M-mode Doppler image obtained from our Doppler model. The positive velocity value indicates the flow direction from the mitral to the apex. The slope of black line represents the flow propagation velocity for the E-waves. The estimated propagation velocity is about 31 cm/s. (b) Mitral center line velocity data obtained directly from the flow simulation.

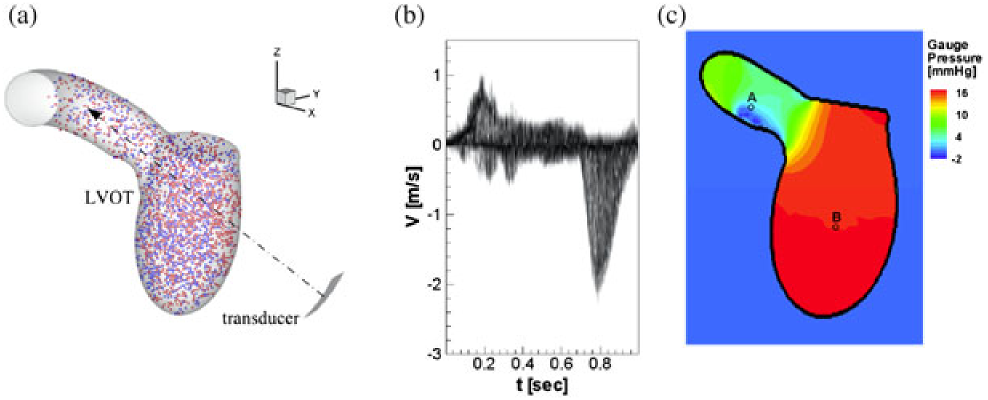

Figure 9. (a) Transducer position and the direction of ultrasound wave beam for continuous wave Doppler. (b) Simulated continuous wave Doppler diagram for the left ventricle outflow tract. (c) Instantaneous gauge pressure contours at $t = 0.8$ s on the plane tangent to the direction of ultrasound wave beam. Point A is the location of maximum blood flow velocity.

ventricular hemodynamics (e.g. LV axial pressure gradient) and $\mathrm{v_p}$ or $\mathrm{v_E/v_p}$. These will be pursued in a future study.

Finally, we demonstrate the generation of a CW Doppler image using our modeling procedure. This mode of ultrasound operation is particularly useful when the primary interest is determining extreme values of velocity in the path of the beam. Clinical applications include determining flow velocity in peripheral arteries and estimation of blood flow and pressure in the left ventricular outflow tract and aorta [9]. For this demonstration we focus on the left ventricle outflow tract (LVOT) which is particularly relevant to pathologies such as obstructive hypertrophic cardiomyopathy (HOCM). For this condition, CW Doppler is used to find the maximum blood flow velocity in the LVOT. Once the maximum velocity is obtained, the LVOT pressure gradient is evaluated by a simplified Bernoulli equation; $\Delta P[\mathrm{mmHg}] = 4(V[\mathrm{m/s}])^2$. The LVOT pressure gradient is an important factor in diagnosing the significance of aortic stenosis or HOCM in the LVOT.

In our model, the transducer of the same shape as described earlier is placed on the location shown in Figure 9(a) and the direction of ultrasound beam is aligned with the blood flow direction in LVOT. The CW Doppler image is obtained from the spectrogram of the received signal and plotted in Figure 9(b). Because the CW scans all the blood volume that lies in the path of the ultrasound beam, the Doppler signal detects an entire range of velocity values at any given time-instance. In our model, the negative peak around 0.8 s (see Figure 9(b)) is the maximum blood flow velocity through the LVOT during the ejection and the value is about 2.1 m/s. The maximum LVOT pressure gradient estimated by the simplified Bernoulli equation is 17.6 mmHg. Figure 9(c) shows the instantaneous pressure field on the plane tangent to the direction of ultrasound wave beam obtained by the computational hemodynamic simulation. Point A is the location of the maximum blood flow velocity and the maximum velocity value is 2.18 m/s which is very close to the value obtained by the CW Doppler. The pressure difference computed directly in the flow simulation between point A and point B (i.e., LVOT pressure gradient) is however about 15 mmHg. Thus the LVOT pressure gradient is slightly over predicted by $4V^2$, a tendency that has also been reported from the *in-vivo* assessments of this technique [9]. Note however that while the pressure inside the LV is almost spatially uniform, the pressure in the aorta varies noticeably based on location. Thus, the present computational hemodynamics and Doppler ultrasound simulation approach can perform a critical assessment of the LVOT pressure gradient estimation. This will be pursued for the sub-aortic LVOT obstruction in the further study.

3.5. *Simulation of systolic ejection murmur*

Heart sound contains important information regarding the health of the cardiac system and auscultation has been used as a noninvasive diagnostic modality for heart disease for many thousands of

DOI: 10.1002/cnm

years. In PC, heart sounds are recorded using an electronic-stethoscope and the resulting phonocardiogram is analyzed in order to detect abnormal heart sounds associated with heart disease [11]. However, the correlation between heart disease, flow patterns and heart sounds is still not fully understood. This is primarily due to the fact that there exist no measurement techniques that can measure ventricular flow patterns and the corresponding heart sounds simultaneously. Thus, a computational technique that can enable the generation of such correlations could have a significant impact on the clinical technique of PC. The application of such correlations run the gamut of heart disease including but not limited to innocent/functional murmurs in children [40], sounds of diastolic dysfunction [13], and systolic murmurs [10] associated with mitral regurgitation aortic and LVOT obstruction.

In the current study, we predict the generation of abnormal heart sound through direct computation of flow and sound and use this to generate a virtual phonocardiogram. In particular, we consider here a systolic ejection murmur caused by a hypertrophic (obstructive) cardiomyopathy (HOCM). It is generally believed that the systolic ejection murmur is generated by the blood flow disturbances due to an obstruction in left-ventricular outflow tract (LVOT) [10] and, in the present study we compute directly the generation and propagation of the murmurs associated with HOCM.

A simplified two-dimensional model of the LV with the ascending aorta is constructed to simulate the flow and associated murmurs during systole (Figure 10(a)). Here, $D_A = 2$ cm, $d_T = 7$ cm, $D_{LV} = 6.4$ cm, and $L_{LV} = 7.4$ cm (at the beginning of systole). A sub-aortic, obstructive hypertrophy is modeled as shown in Figure 10 for the HCM cases. In addition to a normal case, we considered two HCM cases, HCM1 and HCM2, and HCM2 has more severe obstruction than HCM1. For the HCM cases, the mitral valve leaflets are elongated and migrated toward the outflow tract to mimic systolic anterior motion (SAM) which manifests in many severe cases of HCM [41]. In reality, the elongated mitral leaflet can fluctuate along with the flow instability and it may generate additional sound associated with flow-structure interaction. In the present study, however, such a dynamic motion of the leaflets is not considered, and we focus on the flow noise source caused by the obstruction. It is also assumed that the two HCM cases have the same degree of SAM. The resulting gap size in the outflow tract is about $0.3\mathrm{D_A}$ for HCM1 and $0.2\mathrm{D_A}$ for HCM2. The simulations are performed for only the systolic phase of the cardiac cycle. The temporal blood flow rate profile is given in Equation (14), but the systolic period (t_{ES}-t_{SS}) of 0.25 s is used here. The blood flow domain inside the LV and aorta (indicated by shaded area in Figure 10) is resolved by 256 × 384 nonuniform Cartesian grid (see Figure 10(b)) with the minimum grid spacing of $0.015\mathrm{D_A}$. The flow simulation is performed by solving Equations (1-4).

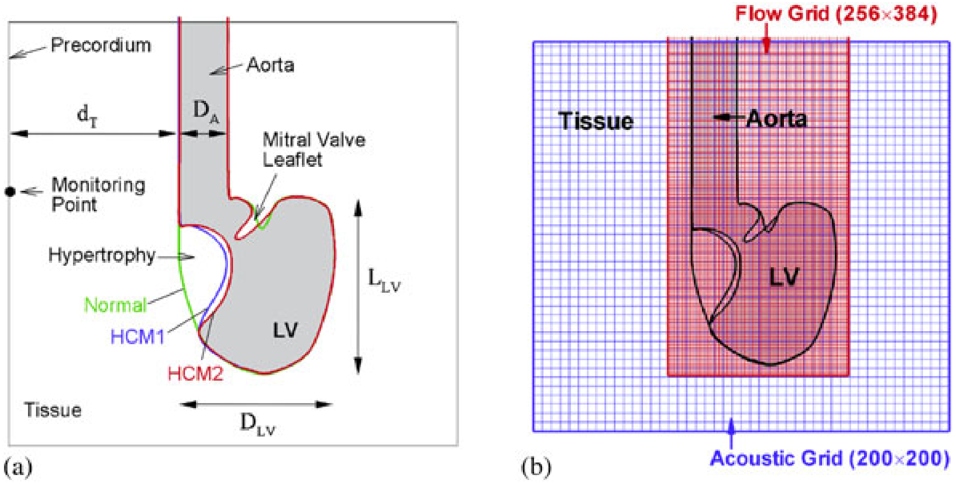

Figure 10. (a) Schematic diagram of simplified left ventricle model with hypertrophy for the computation of systolic ejection murmur. The shaded area (for HCM2 case) indicates the flow domain and $H = 1$ region for Equation (13), whereas $H = 0$ for white area. (b) Computational domains and grids for the flow and acoustic simulations. Every fourth grids are plotted for the clarity.

The sound generation by the blood flow and its propagation in blood and tissue regions are resolved by the acoustic equations, Equation (13). Thus the acoustic domain includes the LV and aorta as well as nearby thoracic region represented by the box in Figure 10(a). The acoustic computation is performed on a separate grid which consists of 200×200 grid points (see Figure 10(b)) with a minimum grid spacing of 0.04D$_A$. The flow simulation results are interpolated onto the acoustic grid in the LV and aorta region using a bi-linear interpolation. The density and speed of sound for the blood are set to 1.05 (g/cm^3) and 1500 (m/s), respectively. For the present simplified thorax model, a thoracic region outside the heart is assumed to consist of a homogeneous tissue material and its density and speed of sound are assumed to be 1.2 (g/cm^3) and 1800 (m/s). These values are averaged material properties of various components in the thorax [42]. The density and speed of sound (i.e., the bulk modulus, $K = \rho c^2$) scales with the amplitude of acoustic pressure fluctuation ($p' \sim K$) and the wavelength ($\lambda = f/c$, where f is the frequency) in an open space. In the PC, the waveform of acoustic signal is primarily used to identify the types of murmur [10]. For a typical frequency range of a murmur (∼O(100) Hz), the wavelength is much longer than any length scales in the thorax for $c > 100$ (m/s), and thus the waveform of murmur is not so sensitive to the slight change in the bulk modulus. The left boundary of the acoustic domain represents the precordium surface and the heart sound is monitored there as is done in actual auscultation. Because a stethoscope senses transmitted sound via the velocity (or acceleration) of the precordium surface [43], we have recorded the velocity fluctuations on the monitoring points shown in Figure 10(a). The zero-stress boundary condition is applied at the precordium surface and it is assumed that acoustic waves radiate through all other boundaries.

The instantaneous hemodynamic flow fields for normal, HCM1, and HCM2 cases are shown in Figure 11 with the vorticity contours. For the normal case, there is no significant vortex motion in the LVOT and aorta. With HCM and SAM, however, the formation of a jet in the gap between the hypertrophy and the mitral valve leaflet is observed and the jet shear layer rolls into vortices which interact with the aortic wall. This complex vortex motion is supposed to be the source of murmur sound. For the smaller gap (HCM2), the blood flow velocity through the gap is faster and exhibits stronger vortex motions.

The acoustic fields are computed by Equation (13) using the computed flow field and pressure. Figure 12 shows the root-mean-squared acoustic fields for the HCM2 case. Interestingly, it seems that the dominant sound originates from the ventricle region rather than the aorta. The velocity fluctuations monitored on the precordium surface are plotted in Figure 13(a) for HCM1 and HCM2 cases. For normal case, no significant velocity fluctuation is observed. Figure 13(a) is the recorded murmur signal for the cases with HCM and can be considered as a virtual phonocardiogram for the HCM murmur. The present simulated murmur signal exhibits an ascendo/descendo configuration [10] (especially for HCM2) which is quite common in systolic murmurs. Note that, with larger

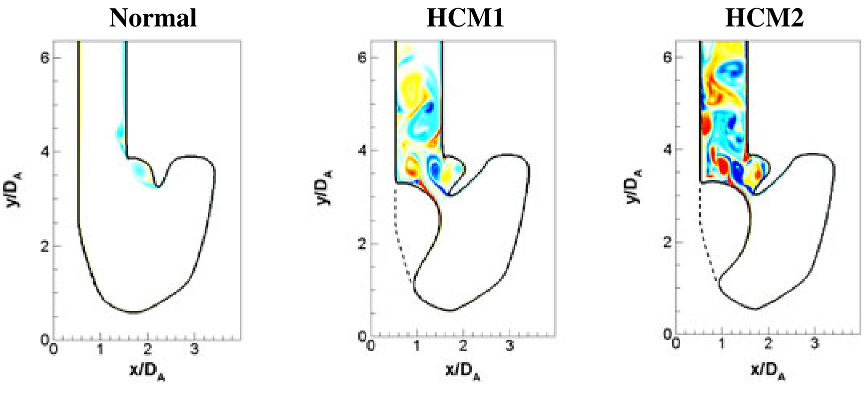

Figure 11. Instantaneous hemodynamic flow field for the normal and hypertrophic cardiomyopathy (HCM) cases represented by vorticity contours at $t = 0.13$ s ($t = 0$ is the start of systole phase).

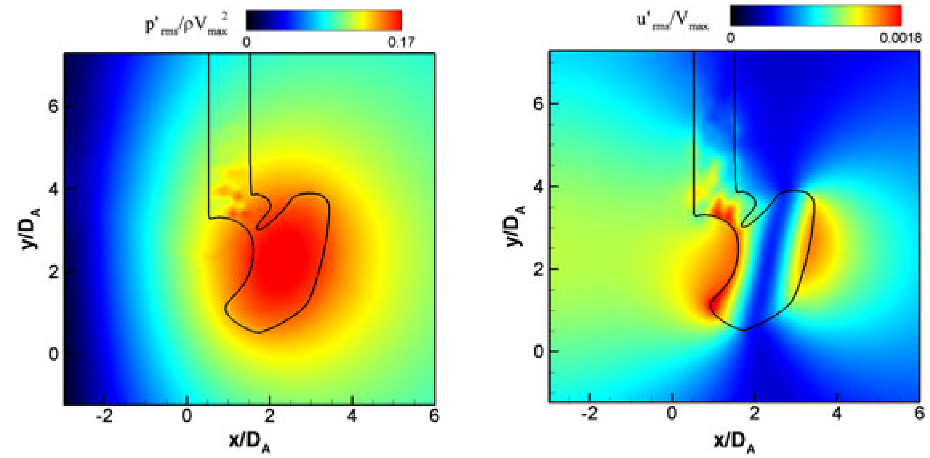

Figure 12. Acoustic fields of hypertrophic cardiomyopathy (HCM) systolic murmur for HCM2 case. Root-mean-squared acoustic pressure fluctuation (left) and x-direction velocity fluctuation (right) contours. Here, $V_{\max}$ is the peak averaged blood flow velocity in the aorta exit during the systole.

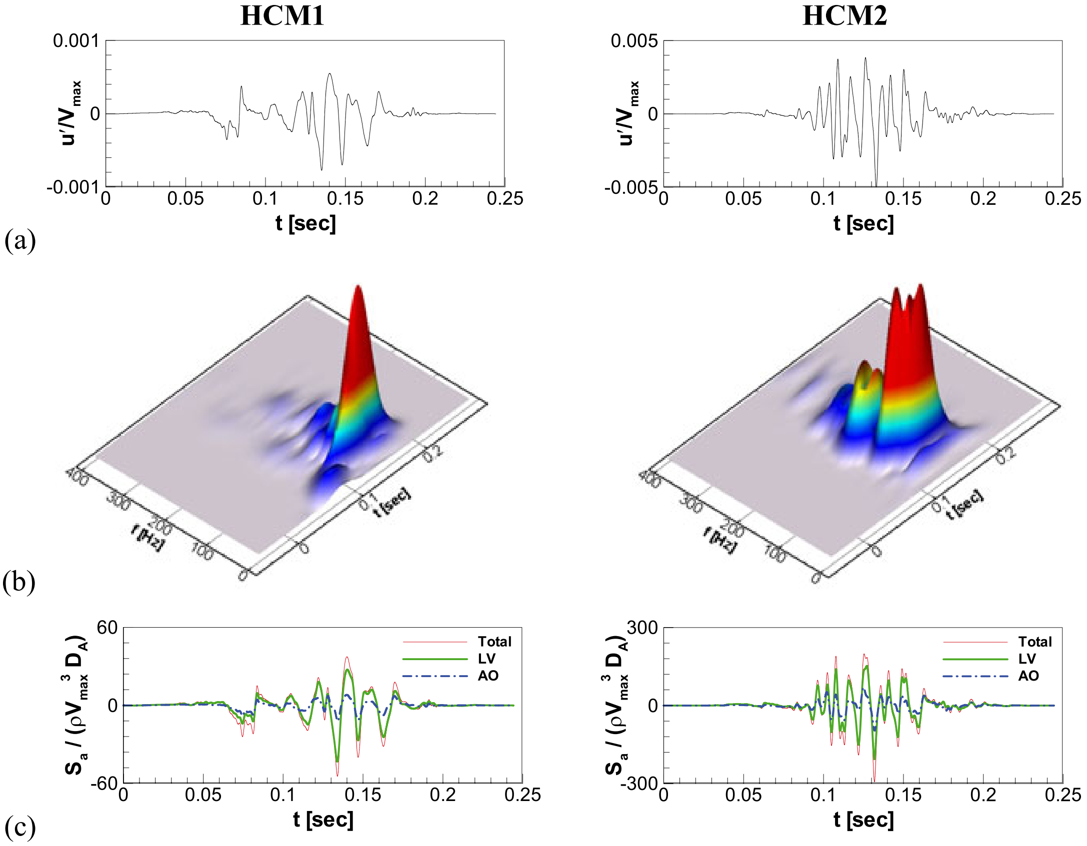

Figure 13. (a) Acoustic velocity fluctuation monitored on the precordium surface. Time signal band-pass filtered for 20–400 Hz. (b) Time-frequency spectrogram. (c) Evaluated source term; volume integrated hydrodynamic pressure fluctuation, $S_a = \int (DP/Dt)\,\mathrm{d}V$ LV: integration over the LV region, AO: integration over the aorta region.

hypertrophy (HCM2), a stronger murmur is generated. Figure 13(b) shows the time-frequency spectrograms of the murmur signals. The strongest energy is found at 64 Hz for HCM1 and 110 Hz for HCM2. HCM2 case also has higher frequency components. Thus in the present results the more severe HCM produces stronger and higher frequency murmur sound.

DOI: 10.1002/cnm

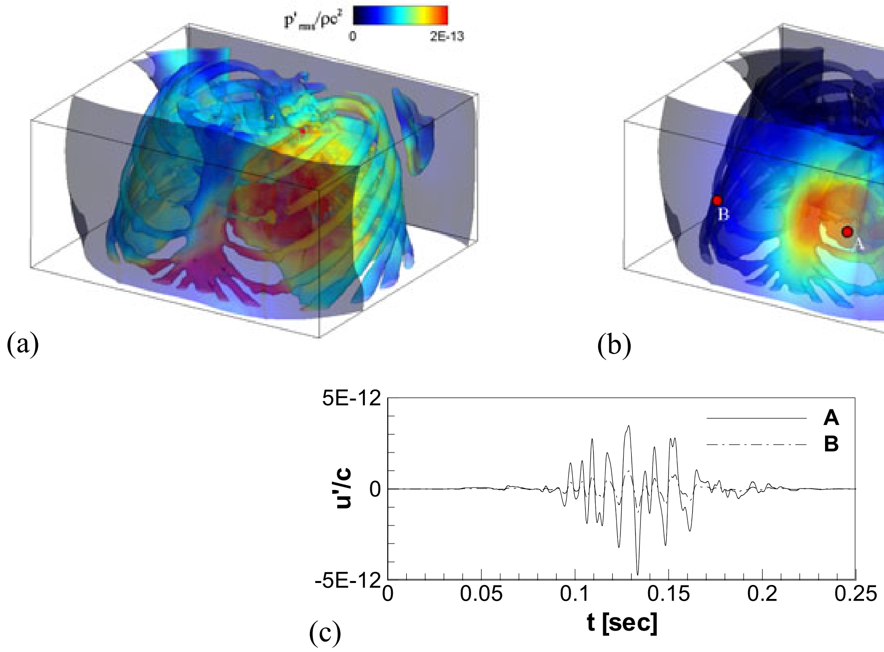

Figure 14. Propagation of systolic HCM murmur computed with a realistic human thorax model. (a) and (b) Root-mean-squared acoustic pressure and velocity fluctuations plotted on the density iso-surfaces. (c) Phonocardiac signals for the hypertrophic cardiomyopathy (HCM) systolic murmur monitored on points A and B in Figure 14(b). The signals are band-pass filtered for 20–400 Hz. Here, ρ and c are the density and the speed of sound of the blood.

Based on the acoustic equation (Equation 13), we have found that the murmur is in fact correlated with the volume integrated hydrodynamics pressure fluctuation. Thus we define the source term; $S_a(t) = \int (DP/Dt)(\vec{x},t)\,\mathrm{d}V$, and it is plotted in Figure 13(c). In order to identify the primary source region of the murmur, we evaluated S_a for the LV and aorta regions separately. One can see that the time signal of S_a is correlated very well with the murmur signal, and the primary contribution to this source term comes from the LV region rather than the aorta, which is inline with the result shown in Figure 12.

Now in order to examine the effect of heart sound propagation in a real human thorax which includes many different biological materials such as chest bones and lungs, we have considered a three-dimensional realistic human thorax model. The model is constructed based on the Visible Human®[‡] Dataset. For the simulation of sound propagation, the contrast value on the CT scan images is converted to the material density and speed of sound using the formulation proposed in Ref. [29]. The density varies from 0.1 g/cm^3 to 2.0 g/cm^3, and we truncated the values that are out of this range. The speed of sound varies from 292 m/s to 2914 m/s. These three-dimensional density and speed of sound fields are mapped on the Cartesian grid of 140×160×80 grid points with the grid spacing of 2.175 mm. Equation (13) is solved with H=0, but the source term, *DP/Dt* on the right hand side is kept. For the sound source, we use *DP/Dt* value on the LV obtained from the hemodynamic flow field simulation of HCM2 case.We first calculate the volume average of *DP/Dt* over the ventricle, $\overline{(DP/Dt)}\,(t) = \int (DP/Dt)(\vec{x},t)\,\mathrm{d}V / \int \mathrm{d}V$ and this source term is placed inside the thorax model at a location typical for the LV as a distributed point source: $(DP/Dt)_{LV}(\vec{x},t) = \overline{(DP/Dt)}\,(t) \times \exp(-\left|\vec{x}-\vec{x}_{LV}\right|^2/r_w^2)$, where $\vec{x}_{LV}$ is the position vector to the center of LV on the thorax model and $r_w = 1$ cm. Figure 14(a) and (b) show the root-mean-squared acoustic fields of HCM murmur radiated in the realistic thorax model. One can clearly see

---

[‡] An anatomical data set developed under a contract from the National Library of Medicine by the Departments of Cellular and Structural Biology, and Radiology, University of Colorado School of Medicine

the high pressure fluctuation around the heart location and high velocity fluctuation on the chest surface above the heart. The velocity fluctuations are monitored on the two locations A and B shown in Figure 14(b) and plotted in Figure 14(c). Figure 14(c) is thus the virtual phonocardiogram of HCM murmur predicted with the realistic thorax model. The point A is on the chest surface directly above the heart, thus the signal monitored at this point shows higher amplitude than point B. Interestingly, the signal monitored at point A looks very similar with the result of simplified thorax model shown in Figure 13(a)(HCM2). This implies that the effect of sound propagation in heterogeneous medium is not so significant for the present low frequency signal ($\sim$O(100) Hz). This observation agrees with the result of Narasimhan *et al*. [29].

The present coupled computational hemodynamic-hemoacoustic approach for the virtual phonocardiogram can be used for a comprehensive investigation of the heart sound generation mechanism and it has the potential to improve the diagnostic ability of the cardiac auscultation. The present method will also be applied to the third and fourth heart sounds [13] to reveal the generation mechanism of those abnormal heart sounds.

4. CONCLUSION

In the current study, methods for the modeling and simulation of intraventricular blood flows, Doppler ultrasound, and blood flow induced heart sound are presented. Blood flow is modeled using a high-fidelity, immersed boundary based Navier–Stokes solver. Virtual ECHO and PC signals are constructed from results of computational hemodynamic simulations by modeling the physics of Doppler ultrasound and heart sound, respectively. The reconstruction of mitral inflow diagram, color M-mode Doppler, and CW Doppler in the left-ventricular outflow tract, and the simulation of systolic HCM murmur are demonstrated, and the possible applications of these virtual cardiographies are also discussed. These virtual cardiographic data not only provide new ways to interpret computational hemodynamic results but also allows us to investigate the correlation between the diagnostic data and specific features of the hemodynamic flow patterns. The development of comprehensive correlations between blood flow dynamic and cardiographic output parameters obtained from the current multi-phyiscs modeling approach is expected to provide new insights into the diagnosis and assessment of a variety of heart conditions.

ACKNOWLEDGEMENTS

This research is supported by the CDI program at NSF through grant IOS-1124804. This work used the Extreme Science and Engineering Discovery Environment (XSEDE), which is supported by NSF grant number TG-CTS100002. The Visible Human® Dataset was provided by the National Library of Medicine. The authors also thank Dr. Albert C. Lardo for providing the contrast CT scan data of the LV

REFERENCES

1. Domenichini F, Pedrizzetti G, Baccani B. Three-dimensional filling flow into a model left ventricle. *Journal of Fluid Mechanics* 2005; **539**:179–198.
2. Mihalef V, Ionasec R, Sharma P, Georgescu B, Voigt I, Suehling M, Comaniciu D. Patient-specifc modelling of whole heart anatomy, dynamics and hemodynamics from four-dimensional cardiac CT images. *Journal of the Royal Society Interface Focus* 2011; **1**:286–296.
3. Saber NR, Gosman AD, Wood NB, Kilner PJ, Charrier CL, Firmin DN. Computational Flow modeling of the left ventricle based on in vivo MRI data: Initial experience. *Annals of Biomedical Engineering* 2001; **29**:275–283.
4. Saber NR, Wood NB, Gosman AD, Merrifield RD, Yang G, Charrier CL, Gatahouse PD, Firmin DN. Progess towards patient speci?c computational flow modeling of the left heart via combination of magnetic resonance imaging with computational fluid dynamics. *Annals of Biomedical Engineering* 2003; **31**:42–52.
5. Schenkel T, Malve M, Markl M, Jung B, Oertel H. MRI-based CFD analysis of flow in a human left ventricle methodology and application to a healthy heart. *Annals of Biomedical Engineering* 2009; **37**(3):505–515.
6. Watanabe H, Sugiura S, Kafuku H, Hisada T. Multiphysics simulation of left ventricular filling dynamics using fluid-structur interaction finite element method. *Biophysical Journal* 2004; **87**:2074–2085.
7. Garcia JM, Smedira NG, Greenberg NL, Main M, Firstenberg MS, Odabashian J, Thomas JD. Color M-mode Doppler flow propagation velocity is a preload insensitive index of left ventricular relaxation: animal and human validation. *Journal of the American College of Cardiology* 2000; **35**:201–208.

8. Nishimura RA, Tajik A. Evaluation of diastolic filling of left ventricle in health and disease: Doppler Echocardiography is the Clinician's Rosetta Stone. *Journal of the American College of Cardiology* 1997; **30**:8–18.
9. Sasson Z, Yock PG, Hatle LK, Alderman EL, Popp RL. Doppler echocardiographic determination of the pressure gradient in hypertrophic cardiomyopathy. *Journal of the American College of Cardiology* 1988; **11**:752–756.
10. Alpert MA. Systolic murmurs. In *Clinical Methods: The History, Physical, and Laboratory Examinations*, Walker HK, Hall WD, Hurst JW (eds), Chapter 2, 3rd Ed. Boston: Butterworths, 1990.
11. Erne P. Beyond auscultation - Acoustic cardiography in the diagnosis and assessment of cardiac disease. *Swiss Medical Weekly* 2008; **138**:439–452.
12. Murgo JP. Systolic ejection murmur in era of modern cardiology, what we really know? *Journal of the American College of Cardiology* 1998; **32**(6):1596–1602.
13. Ronan JA, Jr. Cardiac auscultation: the third and fourth heart sounds. *Heart Disease and Storke* 1992; **1**(5):267–270.
14. Boeck BWL, Oh JK, Vandervoort PM, Vierendeels JA, Aa RPLM, Cramer MJM. Color M-mode velocity propagation: a glance at intra-ventricular pressure gradients and early diastolic ventricular performance. *The European Journal of Heart Failure* 2005; **7**:19–28.
15. Mittal R, Dong H, Bozkurttas M, Najjar FM, Vargas A, von Loebbecke AA. A versatile sharp interface immersed boundary method for incompressible flows with complex boundaries. *Journal of Computational Physics* 2008; **227**:4825–4852.
16. Oung H, Forsberg F. Doppler ultrasound simulation model for pulsatile flow with non-axial components. *Ultrasonic Imaging* 1996; **18**:157–172.
17. Seo JH, Moon YJ. Linearized perturbed compressible equations for low Mach number aeroacoustics. *Journal of Computational Physics* 2006; **218**:702–719.
18. Chorin AJ. On the convergence of discrete approximations to the Navier–Stokes equations. *Mathematics of Computation* 1969; **23**(106):341–353.
19. Bozkurttas M, Dong H, Seshadri V, Mittal R, Najjar F. Towards numerical simulation of flapping foils on fixed Cartesian grids. *43th AIAA Aerospace Sciences Meeting and Exhibition,* Jan. 10-13, AIAA Paper 2005-0081, Reno, Nevada, 2005.
20. McQueen DM, Peskin CS. *Heart Simulation by An Immersed Boundary Method with Formal Second-Order Accuracy and Reduced Numerical Viscosity, Mechanics for a New Mellennium*. Kluwer Academic Publisher: New York, 2002; pp. 429-444.
21. Peskin CS, McQueen DM. A three-dimensional computational method for blood flow in the heart I. Immersed elastic fibers in a viscous incompressible fluids. *Journal of Computational Physics* 1989; **81**(2):372–405.
22. Jensen JA, Svendsen NB. Calculation of pressure fields from arbitrarily shaped, apodized, and excited ultrasound transducers. *IEEE Transactions on Ultrasonics, Ferroelectrics and Frequency Control* 1992; **30**:262–267.
23. Tan L, Jiang J. *Fundamental of: Analog and Digital Signal Processing*. AuthorHouse: Bloomington, Indiana, USA, 2007; pp. 279.
24. Moon YJ, Seo JH, Bae YM, Roger M, Becker S. A hybrid prediction method for low-subsonic turbulent flow noise. *Computers & Fluids* 2010; **39**:1125–1135.
25. Seo JH, Mittal R. A high-order immersed boundary method for acoustic wave scattering and low Mach number flow induced sound in complex geometries. *Journal of Computational Physics* 2011; **230**:1000–1019.
26. Seo JH, Mittal R. A coupled flow-acoustic computational study of bruits from a modeled stenosed artery. *Medical & Biological Engineering & Computing* 2012; **50**:1025–1035.
27. Okita K, Ono K, Takagi S, Matsumoto Y. Development of high intensity focused ultrasound simulator for large-scale computing. *International Journal for Numerical Methods in Fluids* 2010; **65**:43–66.
28. Baron C, Aubry JF, Tanter M, Meairs S, Fink M. Simulation of intracranial acoustic fields in clinical trials sonothrombolysis. *Ultrasound in Medicine & Biology* 2009; **35**(7):1148–1158.
29. Narasimhan C, Ward R, Kruse KL, Gudatti M, Mahinthakumar G. A high resolution computer model for sound propagation in the human thorax based on the Visible Human data set. *Computers in Biology & Medicine* 2004; **34**:177–192.
30. Lele SK. Compact finite difference schemes with spectral-like resolution. *Journal of Computational Physics* 1992; **103**:16–42.
31. Zheng X, Seo JH, Vedula V, Abraham T, Mittal R. Computational modeling and analysis of intracardiac flows in simple models of the left ventricle. *European Journal of Mechanics - B/Fluids* 2012; **35**:31–39.
32. Jeong J, Hussain F. On the identification of a vortex. *Journal of Fluid Mechanics* 1995; **285**:69–94.
33. Domenichini F, Querzoli G, Genedese AG, Pedrizzetti G. Combined experimental and numerical analysis of the flow structure into the left ventricle. *Journal of Biomechanics* 2007; **40**:1988–1994.
34. Redfield MM, Jacobsen SJ, Burnett JC, Jr., Mahoney DW, Bailey KR, Rodeheffer RJ. Burden of systolic and diastolic ventricular dysfunction in the community; Appreciating the scope of the heart failure epidemic. *The Journal of the American Medical Association* 2003; **289**(2):194–202.
35. Taylor TW, Suga H, Goto Y, Okino H, Yamaguchi T. The effects of cardiac infarction on realistic three-dimensional left ventricular blood ejection. *Transactions of the ASME Journal of Biomechanical Engineering* 1996; **118**: 106–110.
36. Moghadam ME, Bazilevs Y, Hsia TY, Vignon-Clementel IE, Marsden AL. A comparison of outlet boundary treatments for prevention of backflow divergence with relevence to blood flow simulations. *Computational Mechanics* 2011; **48**:277–291.

37. Doenst T, Spiegel K, Reik M, Markl M, Henning J, Nitzsche S, Beyersdorf F, Oertel H. Fluid-dynamics modeling of the human left ventricle: methodology and application to surgical ventricular reconstruction. *The Annals of Thoracic Surgery* 2009; **87**:1187–1195.
38. Kilner PJ, Yang G, Wilkes AJ, Mohiaddin RH, Firmin N, Ycoub MH. Asymmetric redirection of flow through the heart. *Nature Letter* 2000; **404**:759–761.
39. Casandra N, Takahiro O, Pavlos V, William L. Measuring heart filling propagation velocity using the cross wavelet transform. *64th Annual Meeting of the APS Division of Fluid Dynamics,* November 20-22, 2011; abstract #D13.002.
40. Smith KM. The innocent heart murmur in children. *Journal of Pediatric Health Care* 1997; **11**:207–214.
41. Levine RA, Vlahakes GJ, Lefebvre X, Guerrero JL, Cape EG, Yoganathan AP, Weyman AE. Papillary muscle displacement causes systolic anterior motion of the mitral valve, Experimental validation and insights into the mechanism of subaortic obstruction. *Circulation* 1995; **91**:1189–1195.
42. Goss SA, Frizzell LA. Dunn F Dependence of the ultrasonic properties of biological tissue on constituent proteins. *Journal of the Acoustical Society of America* 1980; **67**(3):1041–1044.
43. Borisyuk AO. Noise field in the human chest due to turbulent flow in large blood vessel. *Flow, Turbulence and Combustion* 1999; **61**:269–284.

DOI: 10.1002/cnm